Precision Engineering 36 (2012) 435–443

Contents lists available at SciVerse ScienceDirect

Precision Engineering

journal homepage: www.elsevier.com/locate/precision

Spindle dynamics identification for Receptance Coupling Substructure Analysis

Uttara V. Kumar [a], Tony L. Schmitz [b,*]

[a] Department of Mechanical and Aerospace Engineering, University of Florida, 237 MAE-B, Gainesville, FL 32611, United States
[b] Department of Mechanical Engineering and Engineering Science, University of North Carolina at Charlotte, 164 DCH, Charlotte, NC 28223, United States

ARTICLE INFO

Article history:
Received 26 August 2011
Received in revised form
16 November 2011
Accepted 18 January 2012
Available online 31 January 2012

Keywords:
Machine tool
Milling
Dynamics
Prediction
Modeling

ABSTRACT

In this paper, two techniques are described for experimentally identifying the spindle-machine receptances required for tool point frequency response prediction using Receptance Coupling Substructure Analysis (RCSA). In the RCSA approach, the tool–holder–spindle-machine assembly is separated into three components: the tool, holder, and spindle-machine. The spindle-machine receptances are measured and archived. These receptances are then analytically coupled to beam models that represent the tool–holder. The spindle-machine dynamics are determined using: (1) a synthesis approach where a direct frequency response measurement of a standard artifact inserted in the test spindle is combined with a cross frequency response measurement to calculate the required rotational receptances; and (2) a new Euler–Bernoulli beam approach where the direct frequency response measurement is fit using an assumed (fixed-free) form of each mode within the measurement bandwidth. Experimental results are included for two spindles and four tool–holder combinations. The veracity of the new Euler–Bernoulli beam approach, which requires only a single measurement, reduces noise, and improves tool point dynamics prediction accuracy, is demonstrated.

1. Introduction

Milling process models may be implemented to enable pre-process parameter selection for optimized performance. However, due to the inherent coupling between the tool–holder–spindle-machine structural dynamics and chip formation in milling, the frequency response function (FRF) at the tool point must be known for accurate process performance prediction [1–3]. This model-based, pre-process selection aids in avoiding chatter (unstable machining conditions), improving surface finish, and increasing part accuracy. The required tool–holder–spindle-machine dynamics can be obtained by modal testing. However, for the large number of tool–holder combinations in typical production facilities, the measurements can be prohibitively time-consuming and costly.

Receptance Coupling Substructure Analysis (RCSA) may be applied as an alternative to modal testing for each tool–holder–spindle-machine combination [4–7]. In the RCSA approach, the tool–holder–spindle-machine assembly is considered as three separate components: the tool, holder, and spindle-machine and the individual frequency responses of these components are coupled analytically. The archived measurement of the spindle-machine FRF (or receptance) is coupled to the free-free boundary condition receptances of the tool and the holder derived from Timoshenko beam models [8]. Although significant development work has been completed to improve the tool and holder modeling techniques and to better understand the connection stiffness and damping behavior [9–25], relatively less effort has been expended to improve the identification of the spindle-machine dynamics. In this paper, two approaches for determining the spindle-machine dynamics are compared and the subsequent tool point dynamics prediction accuracy is experimentally evaluated. A new technique, based on analytical Euler–Bernoulli beam receptances, is introduced and it is shown that that the new method: (1) reduces the number of required measurements; (2) eliminates the inherent noise in the alternative finite difference-based approach; and (3) is more robust than the finite difference approach.

2. RCSA background

In the three-component RCSA model applied here, the tool and holder receptances are determined from beam models and the spindle-machine receptances are measured by impact testing. These substructure receptances are then joined analytically to obtain the assembly receptance as reflected at the tool point.

Fig. 1 depicts the three individual components of the tool–holder–spindle-machine assembly: the tool (I), the holder (II), and the spindle-machine (III). Both the tool and holder are described using Timoshenko beam models (based on the geometry and material properties) with free-free boundary conditions

* Corresponding author. Tel.: +1 704 687 8421.
E-mail address: tony.schmitz@uncc.edu (T.L. Schmitz).

0141-6359/$ – see front matter © 2012 Elsevier Inc. All rights reserved.
doi:10.1016/j.precisioneng.2012.01.007

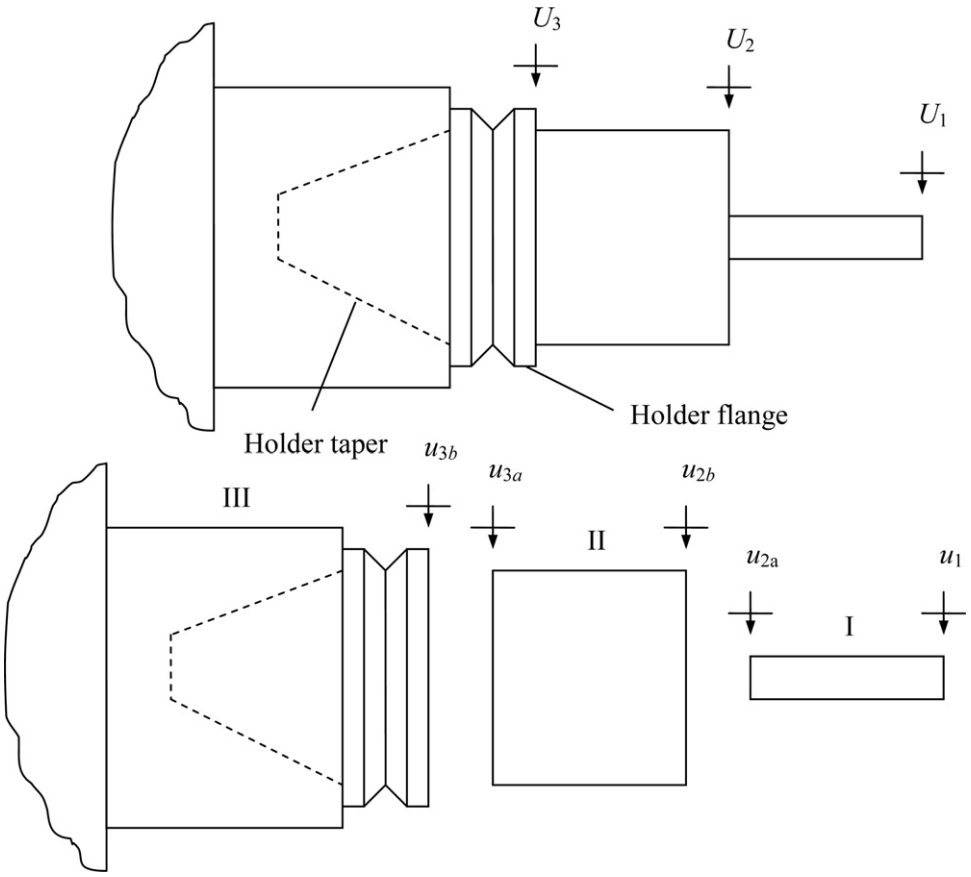

Fig. 1. Three-component receptance coupling model of tool (I), holder (II), and spindle-machine (III).

[8]. The free-free tool and holder models are then coupled to form the subassembly I–II identified in Fig. 2, where $u_i = \left\{ x_i \quad \theta_i \right\}^T$ are the component generalized coordinates composed of both a displacement, x_i, and a rotation, θ_i, and $U_i = \left\{ X_i \quad \Theta_i \right\}^T$ are the assembly generalized coordinates. To couple components I and II, the coordinate definitions provided in Fig. 1 are applied, where $q_i = \left\{ f_i \quad m_i \right\}^T$ are the component generalized forces composed of both a force, f_i, and a moment (or couple), m_i, and $Q_1 = \left\{ F_1 \quad M_1 \right\}^T$ is the assembly generalized force applied at assembly coordinate 1. The component I receptances include: (1) the direct receptances at the free end $h_{11} = (x_1/f_1)$, $l_{11} = (x_1/m_1)$, $n_{11} = (\theta_1/f_1)$, and $p_{11} = (\theta_1/m_1)$; (2) the cross receptances from the free end to the fixed end (connected to the holder) $h_{12a} = (x_1/f_{2a})$, $l_{12a} = (x_1/m_{2a})$, $n_{12a} = (\theta_1/f_{2a})$, and $p_{12a} = (\theta_1/m_{2a})$; (3) the direct receptances at the fixed end $h_{2a2a} = (x_{2a}/f_{2a})$, $l_{2a2a} = (x_{2a}/m_{2a})$, $n_{2a2a} = (\theta_{2a}/f_{2a})$, and $p_{2a2a} = (\theta_{2a}/m_{2a})$; and (4) the cross receptances from the fixed end to the free end $h_{2a1} = (x_{2a}/f_1)$, $l_{2a1} = (x_{2a}/m_1)$, $n_{2a1} = (\theta_{2a}/f_1)$, and $p_{2a1} = (\theta_{2a}/m_1)$. These are organized into the generalized component receptance matrices

$$R_{ij} = \begin{bmatrix} h_{ij} & l_{ij} \\ n_{ij} & p_{ij} \end{bmatrix}$$

where $\{u_i\} = [R_{ij}]\{q_j\}$. For component II, the same receptances must be calculated using the Timoshenko beam model, but coordinate 1 is replaced with 2*b* and coordinate 2*a* is replaced with 3*a*. By assuming a rigid coupling between these two components, the I–II

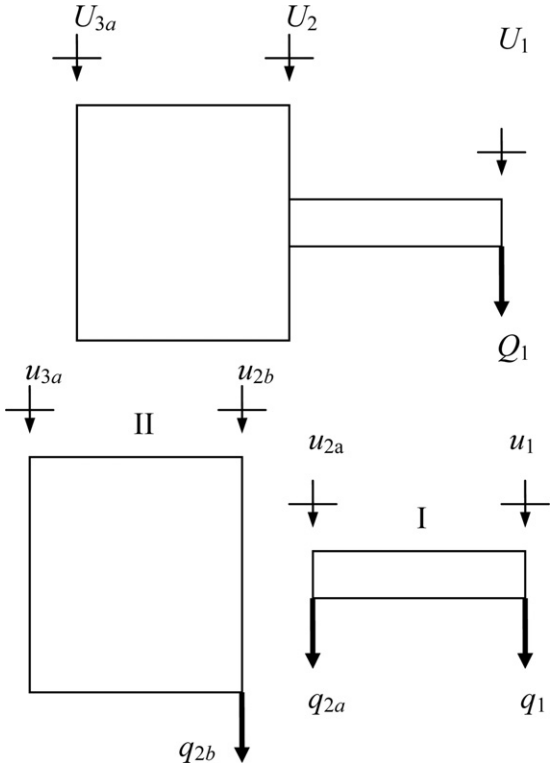

Fig. 2. Subassembly I–II composed of tool (I) and holder (II). The generalized force Q_1 is applied to U_1 to determine G_{11} and G_{3a1}.

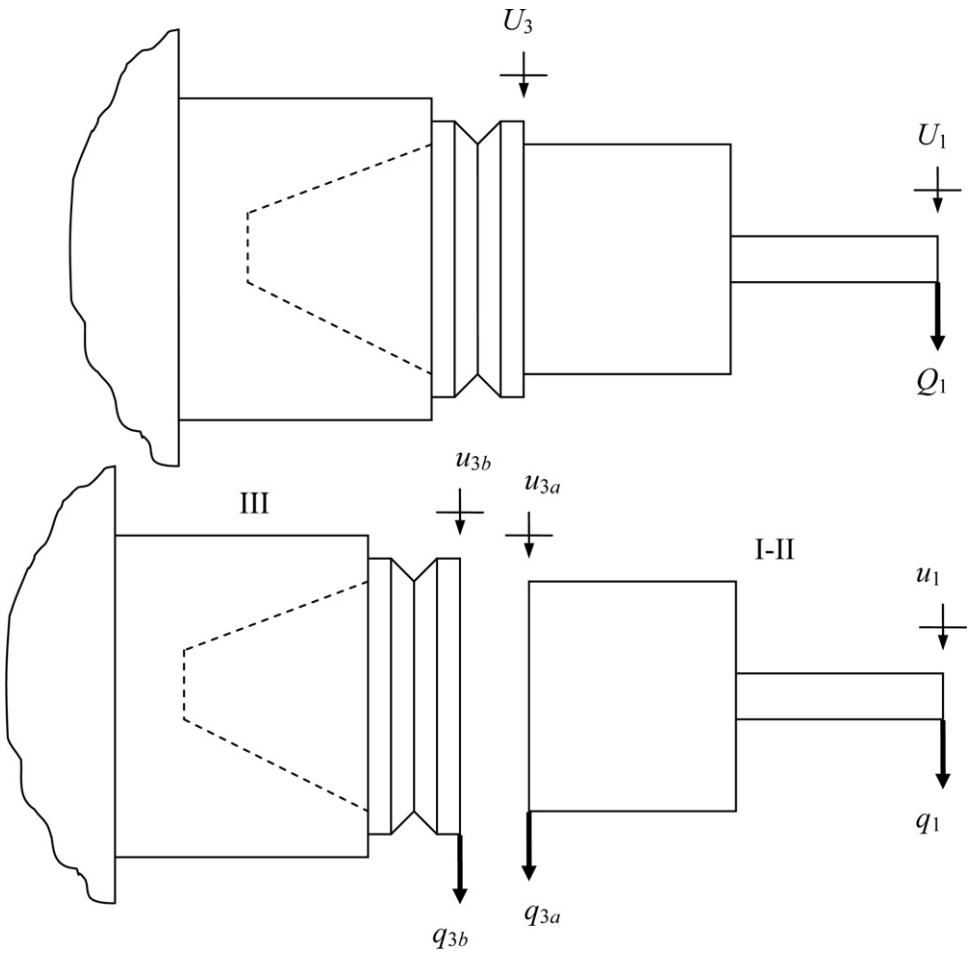

Fig. 3. The I–II subassembly is rigidly coupled to the spindle-machine (III) to determine the tool point receptance matrix, G_{11}.

subassembly tip receptances: (direct) G_{11} and G_{3a3a}; and (cross) G_{13a} and G_{3a1} can be determined, where

$$G_{ij} = \begin{bmatrix} H_{ij} & L_{ij} \\ N_{ij} & P_{ij} \end{bmatrix}$$

are the generalized assembly receptance matrices and $\{U_i\} = [G_{ij}]\{Q_j\}$.

To determine the direct and cross receptances at the right end of the subassembly, G_{11} and G_{3a1}, Q_1 is applied to coordinate U_1 as shown in Fig. 3. The components' displacements/rotations are: $u_1 = R_{11}q_1 + R_{12a}q_{2a}$, $u_{2a} = R_{2a1}q_1 + R_{2a2a}q_{2a}$, $u_{2b} = R_{2b2b}q_{2b}$, and $u_{3a} = R_{3a2b}q_{2b}$. The equilibrium conditions are: $q_{2a} + q_{2b} = 0$ and $q_1 = Q_1$. The component displacements/rotations and equilibrium conditions are substituted into the compatibility condition for the rigid connection, $u_{2b} - u_{2a} = 0$, to obtain the expression for q_{2b} shown in Eq. (1). The component force q_{2a} is then determined from the equilibrium condition $q_{2a} = -q_{2b}$. The expression for G_{11} is provided in Eq. (2). The cross receptance matrix G_{3a1} is shown in Eq. (3).

$$\begin{aligned} &u_{2b} - u_{2a} = 0 \\ &R_{2b2b}q_{2b} - R_{2a1}q_1 - R_{2a2a}q_{2a} = 0 \\ &(R_{2a2a} + R_{2b2b})q_{2b} - R_{2a1}Q_1 = 0 \\ &q_{2b} = (R_{2a2a} + R_{2b2b})^{-1}R_{2a1}Q_1 \end{aligned} \tag{1}$$

$$\begin{aligned} &G_{11} = \frac{U_1}{Q_1} = \frac{u_1}{Q_1} = \frac{R_{11}q_1 + R_{12a}q_{2a}}{Q_1} = \frac{R_{11}Q_1 - R_{12a}(R_{2a2a} + R_{2b2b})^{-1}R_{2a1}Q_1}{Q_1} \\ &G_{11} = R_{11} - R_{12a}(R_{2a2a} + R_{2b2b})^{-1}R_{2a1} = \begin{bmatrix} H_{11} & L_{11} \\ N_{11} & P_{11} \end{bmatrix} \end{aligned} \tag{2}$$

$$\begin{aligned} &G_{3a1} = \frac{U_{3a}}{Q_1} = \frac{u_{3a}}{Q_1} = \frac{R_{3a2b}q_{2b}}{Q_1} = \frac{R_{3a2b}(R_{2a2a} + R_{2b2b})^{-1}R_{2a1}Q_1}{Q_1} \\ &G_{3a1} = R_{3a2b}(R_{2a2a} + R_{2b2b})^{-1}R_{2a1} = \begin{bmatrix} H_{3a1} & L_{3a1} \\ N_{3a1} & P_{3a1} \end{bmatrix} \end{aligned} \tag{3}$$

To find the remaining tip receptances, G_{3a3a} and G_{13a}, Q_{3a} is applied to assembly coordinate U_{3a}. Following the same approach, the equations for the direct receptance G_{3a3a} (Eq. (4)) and the cross receptance G_{13a} (Eq. (5)) are determined.

$$\begin{aligned} &G_{3a3a} = \frac{U_{3a}}{Q_{3a}} = \frac{u_{3a}}{Q_{3a}} = \frac{R_{3a3a}q_{3a} + R_{3a2b}q_{2b}}{Q_{3a}} \\ &G_{3a3a} = \frac{R_{3a3a}Q_{3a} - R_{3a2b}(R_{2a2a} + R_{2b2b})^{-1}R_{2b3a}Q_{3a}}{Q_{3a}} \\ &G_{3a3a} = R_{3a3a} - R_{3a2b}(R_{2a2a} + R_{2b2b})^{-1}R_{2b3a} = \begin{bmatrix} H_{3a3a} & L_{3a3a} \\ N_{3a3a} & P_{3a3a} \end{bmatrix} \end{aligned} \tag{4}$$

$$\begin{aligned} &G_{13a} = \frac{U_1}{Q_{3a}} = \frac{u_1}{Q_{3a}} = \frac{R_{12a}q_{2a}}{Q_{3a}} = \frac{R_{12a}(R_{2a2a} + R_{2b2b})^{-1}R_{2b3a}Q_{3a}}{Q_{3a}} \\ &G_{13a} = R_{12a}(R_{2a2a} + R_{2b2b})^{-1}R_{2b3a} = \begin{bmatrix} H_{13a} & L_{13a} \\ N_{13a} & P_{13a} \end{bmatrix} \end{aligned} \tag{5}$$

Once the free-free components I and II are coupled to form the subassembly I–II, this subassembly is then rigidly coupled to the

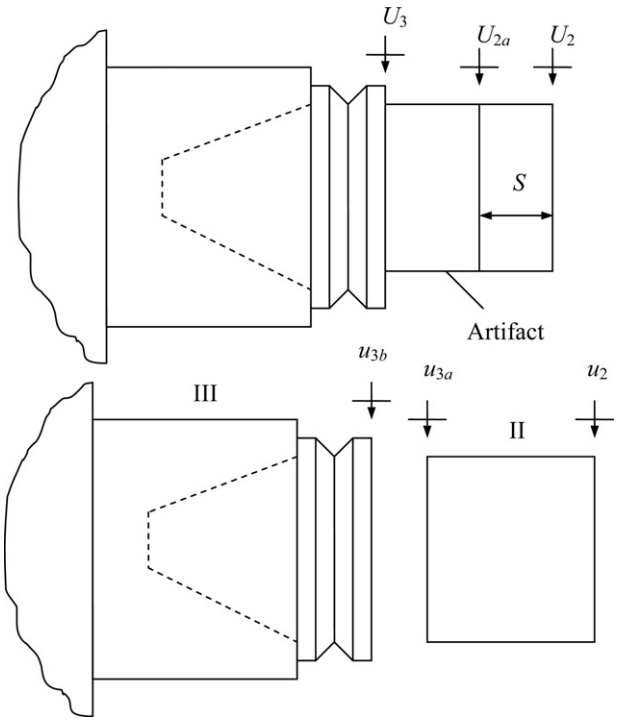

Fig. 4. Artifact model for determining R_{3b3b} by inverse RCSA.

spindle-machine to give the assembly tool point receptances, G_{11}; see Fig. 3. This coupling is carried out using Eq. (6):

$$G_{11} = R_{11} - R_{13a}(R_{3a3a} + R_{3b3b})^{-1}R_{3a1} \tag{6}$$

where the R_{ij} matrices are the subassembly matrices from the I–II coupling result. Therefore, $R_{11} = G_{11}$ from Eq. (2), $R_{3a1} = G_{3a1}$ from Eq. (3), $R_{3a3a} = G_{3a3a}$ from Eq. (4), and $R_{13a} = G_{13a}$ from Eq. (5). The remaining unknown in Eq. (6) is the spindle-machine receptance matrix, R_{3b3b}.

3. Spindle-machine receptances

In order to identify R_{3b3b} for Eq. (6) experimentally, a measurement artifact that includes not only the flange and taper, but also incorporates some length beyond the flange is inserted into the spindle; see Fig. 4. The assembly matrix

$$G_{22} = \begin{bmatrix} H_{22} & L_{22} \\ N_{22} & P_{22} \end{bmatrix}$$

is determined experimentally and then the portion of the artifact beyond the flange is removed in simulation to isolate R_{3b3b}. The free end response for the artifact-spindle-machine assembly is described by Eq. (7), where the R_{22}, R_{23a}, R_{3a3a}, and R_{3a2} matrices are populated using a beam model of the portion of the artifact beyond the flange. Eq. (7) is rearranged in Eq. (8) to isolate R_{3b3b}. This step of decomposing the measured assembly receptances, G_{22}, into the modeled substructure receptances, R_{3a2}, R_{22}, R_{23a}, and R_{3a3a}, and spindle-machine receptances, R_{3b3b}, is referred to as "inverse RCSA". The experimental identification of the four receptances that make up the G_{22} matrix is the focus of this paper.

$$G_{22} = R_{22} - R_{23a}(R_{3a3a} + R_{3b3b})^{-1}R_{3a2} \tag{7}$$

$$\begin{aligned} G_{22} - R_{22} &= -R_{23a}(R_{3a3a} + R_{3b3b})^{-1}R_{3a2} \\ {R_{23a}}^{-1}(R_{22} - G_{22})R_{3a2}^{-1} &= (R_{3a3a} + R_{3b3b})^{-1} \\ R_{3a2}(R_{22} - G_{22})^{-1}R_{23a} &= R_{3a3a} + R_{3b3b} \\ R_{3b3b} &= R_{3a2}(R_{22} - G_{22})^{-1}R_{23a} - R_{3a3a} \end{aligned} \tag{8}$$

3.1. Synthesis approach

In order to define the

$$G_{22} = \begin{bmatrix} H_{22} & L_{22} \\ N_{22} & P_{22} \end{bmatrix}$$

receptances using the artifact in Fig. 4, the direct displacement-to-force term $H_{22} = (X_2/F_2)$ is measured by impact testing.[1] To find the rotation-to-force receptance, $N_{22} = (\Theta_2/F_2)$, a first-order backward finite difference approach [26,27] can be implemented. By measuring both the direct FRF, H_{22}, and cross FRF, $H_{2a2} = (X_{2a}/F_2)$, N_{22} is computed using Eq. (9). The displacement-to-force cross FRF H_{2a2} is obtained by exciting the assembly at U_2 and measuring the response at coordinate U_{2a}, located a distance S from the artifact's free end (see Fig. 4).

$$N_{22} = \frac{H_{22} - H_{2a2}}{S} = \frac{H_{22} - H_{22a}}{S} \tag{9}$$

To obtain a symmetric G_{22} matrix, L_{22} can be assumed to be equal to N_{22}. To find P_{22}, Eq. (10) may be applied, where the measured H_{22} and derived N_{22} receptances are used to synthesize P_{22} [7]. The four receptances required to populate G_{22} are now known and Eq. (8) can be used to obtain R_{3b3b}. Given R_{3b3b}, free-free models for arbitrary tool–holder combinations can be developed and coupled to the spindle-machine receptances to predict the tool point FRF, H_{11}, required for milling process simulation.

$$P_{22} = \frac{\Theta_2}{M_2} = \frac{F_2}{X_2}\frac{X_2}{M_2}\frac{\Theta_2}{F_2} = \frac{1}{H_{22}}L_{22}N_{22} = \frac{N_{22}^2}{H_{22}} \tag{10}$$

3.2. Euler–Bernoulli beam method

As an alternative to completing two measurements on the standard artifact and using the synthesis technique, in this approach a single direct measurement is performed at the free end of the standard artifact. It is then assumed that each mode within the measurement bandwidth can be approximated as a fixed-free beam and the individual modes are fit using the closed-form receptance equation for fixed-free Euler–Bernoulli (E–B) beams presented by Bishop and Johnson [28]. The fit is completed using Eq. (11) for the displacement-to-force receptance at the free end of a cylindrical fixed-free beam, where $\lambda^4 = \omega^2((\rho A)/(EI(1 + i\eta)))$, $A = ((\pi d^2)/4)$, $I = ((\pi d^4)/64)$, ω is frequency (rad/s), ρ is the density, E is the elastic modulus, η is the solid damping factor (unitless), d is the beam diameter, and L is the beam length.

$$H_{22} = \frac{\sin(\lambda L)\cosh(\lambda L) - \cos(\lambda L)\sinh(\lambda L)}{\lambda^3 EI(1 + i\eta)(\cos(\lambda L)\cosh(\lambda L) - 1)} \tag{11}$$

The algorithm for fitting each mode is composed of five steps.

1. Determine the natural frequency, f_n (Hz), for the mode to be fit from the measured H_{22} receptance.

[1] In impact testing, an instrumented hammer is used to excite the structure and a transducer, often a low-mass accelerometer, is used to measure the response. The Fourier transforms of the two time–domain signals are computed. Their frequency–domain ratio gives the desired receptance.

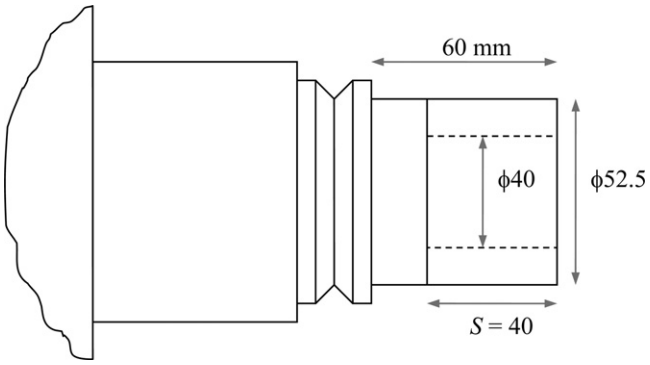

Fig. 5. Artifact dimensions for Cincinnati FTV5-2500 measurements.

2. Select a beam diameter (this is a fitting parameter) and specify the modulus and density (steel values, $E = 200\,\text{GPa}$ and $\rho = 7800\,\text{kg/m}^3$, were used here).
3. Calculate the beam length using the closed-form expression for the natural frequency of a fixed-free cylindrical beam; see Eq. (12) [29].
4. Adjust η to obtain the proper slope for the real part of the mode in question.
5. If the subsequent mode magnitude is too large, increase d to d_{new} and calculate L_{new} using Eq. (13) (to maintain the same natural frequency). If the mode magnitude is too small, decrease d and calculate L_{new}.

$$L = \left(\frac{1.87510407^2 d}{2\pi f_n} \left(\frac{E}{16\rho} \right)^{1/2} \right)^{1/2} \tag{12}$$

$$L_{new} = L \sqrt{\frac{d_{new}}{d}} \tag{13}$$

Once the final fit parameters d, L, and η are determined (the *new* subscript is removed for convenience) and combined with the selected E and ρ values, the remaining receptances for the free end of the artifact are calculated as shown in Eqs. (14) and (15). No additional measurements are required.

$$L_{22} = N_{22} = \frac{-\sin(\lambda L)\sinh(\lambda L)}{\lambda^2 EI(1+i\eta)(\cos(\lambda L)\cosh(\lambda L)-1)} \tag{14}$$

$$P_{22} = \frac{\cos(\lambda L)\sinh(\lambda L)+\sin(\lambda L)\cosh(\lambda L)}{\lambda EI(1+i\eta)(\cos(\lambda L)\cosh(\lambda L)-1)} \tag{15}$$

The four G_{22} receptances are then known and Eq. (8) can be used to obtain R_{3b3b}, the spindle-machine receptances.

4. Results

4.1. Spindle-machine receptances comparison

In this section, the G_{22} receptances identified using the synthesis and E–B approaches are compared. For this example, a Cincinnati FTV5-2500 CNC milling machine spindle (HSK-63A interface) was tested using the steel artifact depicted in Fig. 5. Direct and cross FRFs were measured ($S = 40\,\text{mm}$) using impact testing and the G_{22} identification methods described in Sections 3.1 and 3.2 were completed. The H_{22} measurement and 17 mode E–B fit are presented in Fig. 6; the E–B fitting parameters are provided in Table 1.

The L_{22}/N_{22} receptances were calculated using Eq. (9) for the synthesis technique and Eq. (14) for the E–B approach. The results are compared in Fig. 7. Good agreement in both magnitude and frequency is observed, although the E–B receptance is less noisy due to the fitting step and elimination of the finite difference calculation. The P_{22} receptances obtained using Eqs. (10) (synthesis) and (15) (E–B) are displayed in Fig. 8. Again, the agreement is good except at the anti-resonant frequencies for the higher order modes (near 2100 Hz, 3200 Hz, and 4800 Hz). For the synthesized receptance, the imaginary part exhibits unexpected positive values in these frequency ranges. This is presumably due to the division by the complex-valued receptance, H_{22}, in Eq. (10).

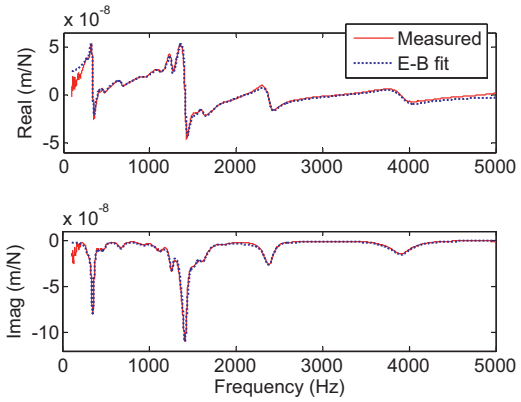

Fig. 6. H_{22} artifact measurement and E–B fit for Cincinnati FTV5-2500 CNC milling machine.

Table 1
E–B fitting parameters for Cincinnati FTV5-2500 CNC milling machine spindle.

Mode	f_n (Hz)	d (m)	η	L (m)
1	280	0.500	0.10	1.1229
2	340	0.175	0.10	0.6029
3	423	0.500	0.07	0.9136
4	464	0.320	0.128	0.6978
5	670	0.280	0.115	0.5432
6	935	0.320	0.11	0.4916
7	1115	0.220	0.09	0.3733
8	1252.5	0.180	0.04	0.3186
9	1365	0.200	0.05	0.3217
10	1408.5	0.092	0.046	0.2148
11	1512	0.170	0.06	0.2818
12	1618	0.135	0.08	0.2427
13	1880	0.30	0.08	0.3357
14	2325	0.246	0.063	0.273
15	2380	0.115	0.05	0.1847
16	2690	0.40	0.07	0.3240
17	3910	0.085	0.08	0.1239

4.2. Tool point receptance prediction comparison

In a second study, the G_{22} receptances were again identified using the synthesis and E–B approaches. These receptances were

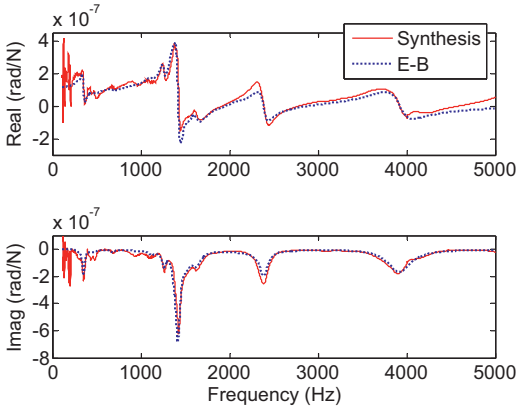

Fig. 7. L_{22}/N_{22} results for the Cincinnati FTV5-2500 CNC milling machine.

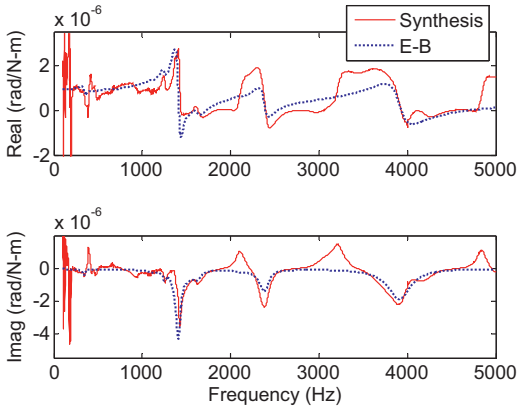

Fig. 8. P_{22} results for the Cincinnati FTV5-2500 CNC milling machine.

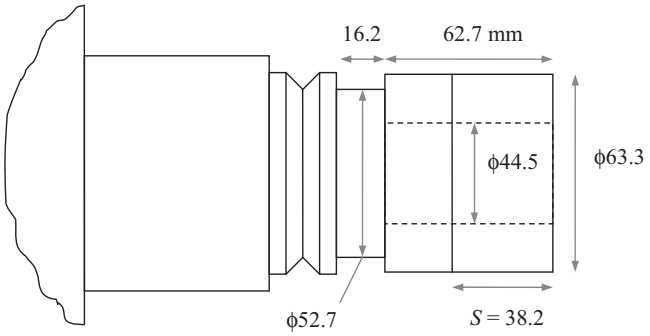

Fig. 9. Artifact dimensions for Mikron UCP-600 Vario measurements.

first used to calculate the R_{3b3b} matrix and then the archived R_{3b3b} receptances were rigidly coupled to Timoshenko beam models of various tool–holder combinations to predict the corresponding tool point H_{11} receptances. These predictions were finally compared to measurement results. In this case, a Mikron UPC-600 Vario CNC milling machine spindle (HSK-63A interface) was tested using the steel artifact depicted in Fig. 9 (S = 38.2 mm). The H_{22} measurement and 24 mode E–B fit are presented in Fig. 10; the E–B fitting parameters are provided in Table 2. The L_{22}/N_{22} receptances are displayed in Fig. 11 and the P_{22} receptances in Fig. 12. The trends are similar to those discussed in Section 4.1.

Given the G_{22} receptances (from the two techniques), the spindle-machine receptance matrices, R_{3b3b}, were calculated using Eq. (8) and a free-free boundary condition Timoshenko beam model

Table 2
E–B fitting parameters for Mikron UPC-600 Vario CNC milling machine spindle.

Mode	f_n (Hz)	d (m)	η	L (m)
1	550	0.375	0.10	0.6950
2	610	0.520	0.06	0.7771
3	703	0.330	0.06	0.5767
4	795	0.450	0.050	0.6160
5	840	0.565	0.035	0.6903
6	875	0.260	0.05	0.4588
7	975	0.107	0.07	0.2788
8	1057	0.208	0.032	0.3734
9	1080	0.255	0.032	0.4090
10	1131	0.107	0.054	0.2589
11	1230	0.173	0.055	0.3157
12	1297	0.206	0.042	0.3354
13	1422	0.196	0.078	0.3125
14	1750	0.200	0.11	0.2845
15	1872	0.115	0.06	0.2086
16	2040	0.190	0.15	0.2569
17	2620	0.220	0.13	0.2439
18	2985	0.098	0.06	0.1525
19	3060	0.125	0.07	0.1701
20	3205	0.185	0.07	0.2022
21	3800	0.270	0.06	0.2244
22	3975	0.340	0.04	0.2462
23	4150	0.220	0.05	0.1938
24	4310	0.112	0.05	0.1357

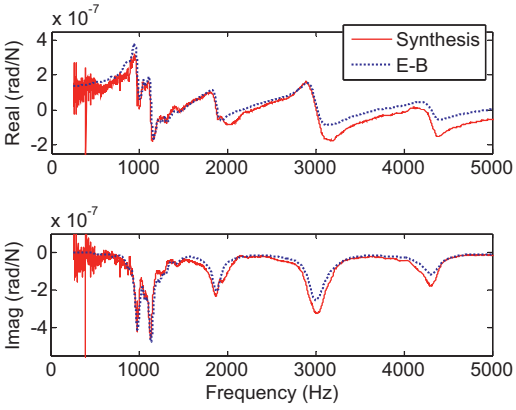

Fig. 11. L_{22}/N_{22} results for the Mikron UCP-600 Vario CNC milling machine.

for the portion of the standard artifact beyond the flange. The dimensions provided in Fig. 9 were used together with steel material properties (E = 200 GPa, ρ = 7800 kg/m^3, and Poisson's ratio ν = 0.29) to develop the artifact model.

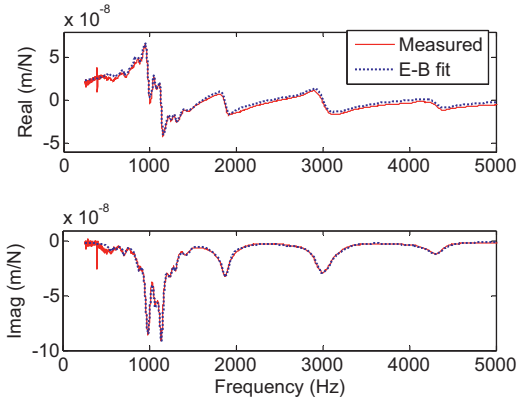

Fig. 10. H_{22} artifact measurement and E–B fit for Mikron UCP-600 Vario CNC milling machine.

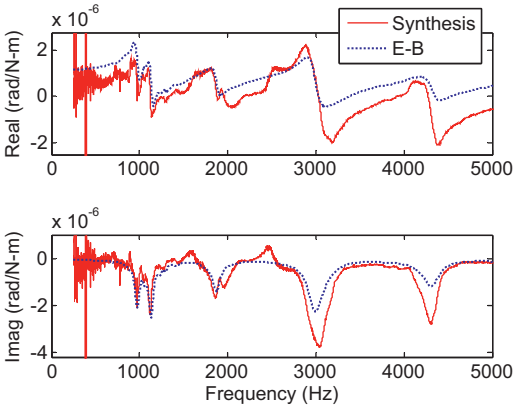

Fig. 12. P_{22} results for the Mikron UCP-600 Vario CNC milling machine.

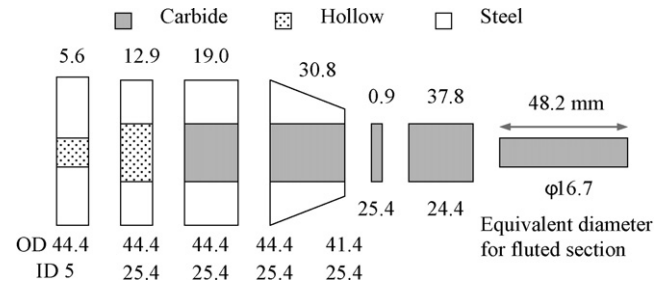

Fig. 13. Beam model for 25.4 mm diameter, three flute endmill inserted in a tapered shrink fit holder (not to scale).

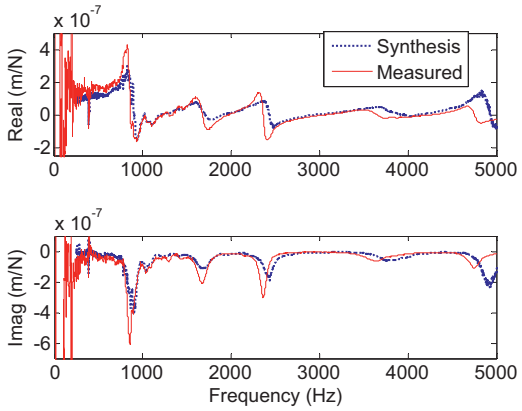

Fig. 14. Comparison between H_{11} tool point measurement and synthesis approach prediction for three flute, 25.4 mm diameter endmill with an overhang length of 86.9 mm.

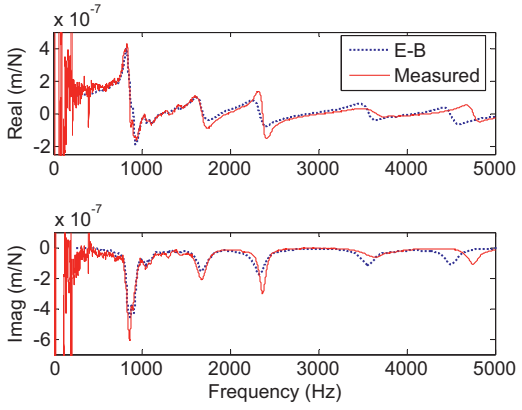

Fig. 15. Comparison between H_{11} tool point measurement and E–B approach prediction for three flute, 25.4 mm diameter endmill with an overhang length of 86.9 mm.

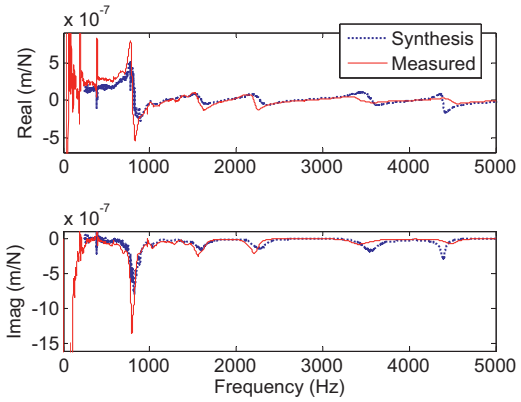

Fig. 16. Comparison between H_{11} tool point measurement and synthesis approach prediction for three flute, 25.4 mm diameter endmill with an overhang length of 107 mm.

4.2.1. 25.4 mm diameter carbide endmill in a shrink fit holder

A three flute, 25.4 mm diameter carbide endmill was clamped in a (thermal) shrink fit tool holder. After inserting this subassembly in the Mikron UCP-600 Vario spindle, the tool point receptance, H_{11}, was measured by impact testing and compared to predictions using the synthesis and E–B R_{3b3b} receptance matrices. The dimensions for the Timoshenko beam tool–holder model are provided in Fig. 13 for an overhang length of 86.9 mm. The fluted portion of the tool was modeled using an equivalent diameter, where this diameter was obtained by weighing the carbide tool, assuming a density (15,000 kg/m^3), and calculating the solid section equivalent flute diameter based on the cylindrical dimensions and the tool and

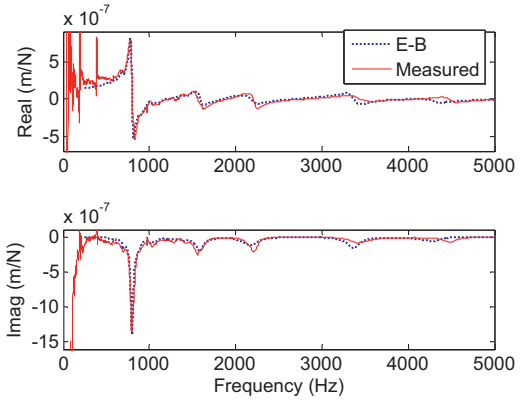

Fig. 17. Comparison between H_{11} tool point measurement and E–B approach prediction for three flute, 25.4 mm diameter endmill with an overhang length of 107 mm.

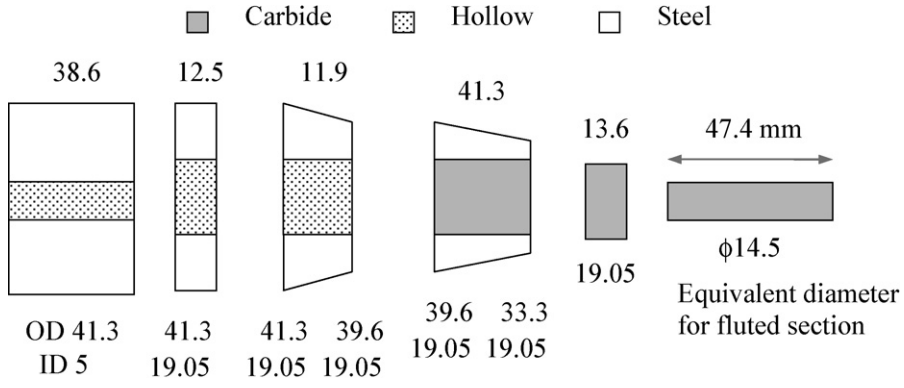

Fig. 18. Beam model for 19.05 mm diameter, four flute endmill inserted in a tapered shrink fit holder (not to scale).

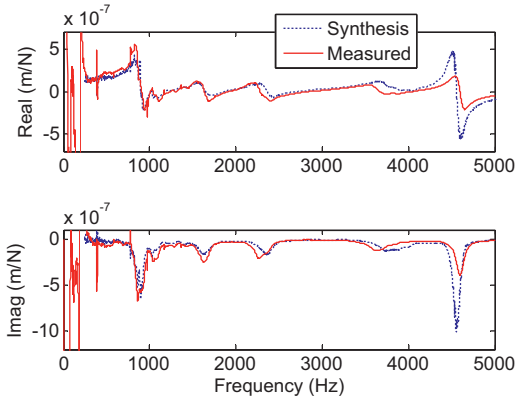

Fig. 19. Comparison between H_{11} tool point measurement and synthesis approach prediction for four flute, 19.05 mm diameter endmill with an overhang length of 61 mm.

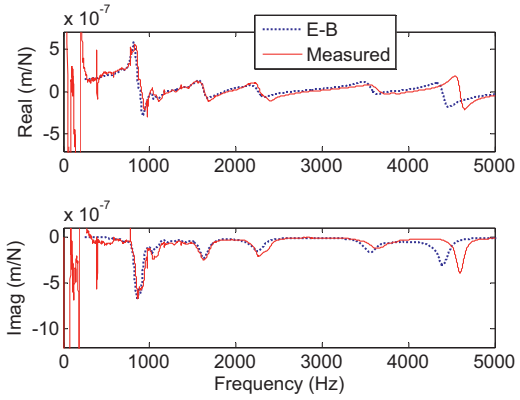

Fig. 20. Comparison between H_{11} tool point measurement and E–B approach prediction for four flute, 19.05 mm diameter endmill with an overhang length of 61 mm.

flute lengths. The elastic modulus for the Timoshenko beam model was 550 GPa and Poisson's ratio was 0.22. The synthesis prediction and measurement are presented in Fig. 14; the E–B prediction and measurement are displayed in Fig. 15. The overhang length was then extended to 107 mm and the exercise was repeated. The results are shown in Figs. 16 and 17. In both cases, the E–B approach slightly outperformed the synthesis technique based on a visual comparison between the predictions and measurements.

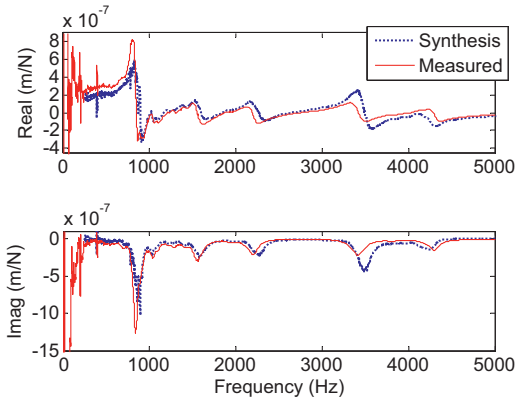

Fig. 21. Comparison between H_{11} tool point measurement and synthesis approach prediction for four flute, 19.05 mm diameter endmill with an overhang length of 76 mm.

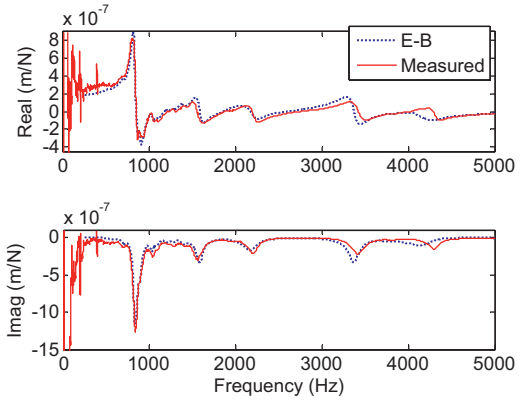

Fig. 22. Comparison between H_{11} tool point measurement and E–B approach prediction for four flute, 19.05 mm diameter endmill with an overhang length of 76 mm.

4.2.2. 19.05 mm diameter carbide endmill in a shrink fit holder

For these tests, a four flute, 19.05 mm diameter carbide endmill was clamped in a shrink fit tool holder and this subassembly was inserted in the Mikron UCP-600 Vario spindle. Tool point measurements were again completed to compare to predictions using the synthesis and E–B R_{3b3b} receptance matrices. The dimensions for the Timoshenko beam tool–holder model are provided in Fig. 18 for an overhang length of 61 mm. The synthesis prediction and measurement are provided in Fig. 19; the E–B prediction and measurement are displayed in Fig. 20. The overhang length was then extended to 76 mm. These results are shown in Figs. 21 and 22. Again, the E–B approach slightly outperformed the synthesis technique.

5. Conclusions

In this study, two approaches were described for experimentally identifying the spindle-machine receptances required for tool point frequency response prediction using Receptance Coupling Substructure Analysis (RCSA). In the RCSA approach, the tool–holder–spindle-machine assembly is separated into three components: the tool, holder, and spindle-machine. The spindle-machine receptances are measured and archived. These receptances are then analytically coupled to beam models that represent the tool–holder. The spindle-machine dynamics were determined using: (1) a synthesis approach where a direct frequency response measurement of a standard artifact inserted in the test spindle is combined with a cross frequency response measurement to calculate the required rotational receptances; and (2) an Euler–Bernoulli beam approach where the direct frequency response measurement is fit using an assumed (fixed-free) form of each mode within the measurement bandwidth. Based on the measurement results presented here, the new Euler–Bernoulli approach appears to adequately describe the spindle-machine response so that accurate tool–holder–spindle-machine assembly predictions may be completed. In comparison with the synthesis technique, the Euler–Bernoulli approach offers the following improvements: (1) a reduction in the number of measurements; (2) reduced noise due to the elimination of the finite differencing step; and (3) improved tool point frequency response function prediction accuracy.

Acknowledgements

The authors gratefully acknowledge financial support from the National Science Foundation through Grant numbers

CMMI-0928393 and CMMI-0928211 (G. Hazelrigg, MCME program manager).

References

[1] Tlusty J. Manufacturing processes and equipment. Upper Saddle River, NJ: Prentice-Hall, Inc.; 2000.
[2] Altintas Y. Manufacturing automation: metal cutting mechanics, machine tool vibrations, and CNC design. Cambridge, UK: Cambridge University Press; 2000.
[3] Schmitz T, Smith KS. Machining dynamics: frequency response to improved productivity. New York, NY: Springer; 2009.
[4] Schmitz T, Donaldson R. Predicting high-speed machining dynamics by substructure analysis. Annals of the CIRP 2000;49(1):303–8.
[5] Schmitz T, Davies M, Medicus K, Snyder J. Improving high-speed machining material removal rates by rapid dynamic analysis. Annals of the CIRP 2001;50(1):263–8.
[6] Schmitz T, Davies M, Kennedy M. Tool point frequency response prediction for high-speed machining by RCSA. Journal of Manufacturing Science and Engineering 2001;123:700–7.
[7] Schmitz T, Duncan GS. Three-component receptance coupling substructure analysis for tool point dynamics prediction. Journal of Manufacturing Science and Engineering 2005;127(4):781–90.
[8] Weaver Jr W, Timoshenko S, Young D. Vibration problems in engineering. 5th ed. New York, NY: John Wiley and Sons; 1990.
[9] Park S, Altintas Y, Movahhedy M. Receptance coupling for end mills. International Journal of Machine Tools and Manufacture 2003;43(9):889–96.
[10] Kivanc EB, Budak E. Structural modeling of end mills for form error and stability analysis. International Journal of Machine Tools and Manufacture 2004;44(11):1151–61.
[11] Duncan GS, Tummond M, Schmitz T. An investigation of the dynamic absorber effect in high-speed machining. International Journal of Machine Tools and Manufacture 2005;45:497–507.
[12] Burns T, Schmitz T. A study of linear joint and tool models in spindle-holder-tool receptance coupling. In: Proceedings of the 2005 American Society of Mechanical Engineers International Design Engineering Technical Conferences and Computers and Information in Engineering Conference, vol. 6: 5th International Conference on Multibody Systems, Nonlinear Dynamics, and Control, Parts A, B, and C. 2005., ISBN 0-7918-4743-8 p. 947–54.
[13] Schmitz T, Duncan GS. Receptance coupling for dynamics prediction of assemblies with coincident neutral axes. Journal of Sound and Vibration 2006;289(4–5):1045–65.
[14] Ertürk A, Özgüven HN, Budak E. Analytical modeling of spindle-tool dynamics on machine tools using Timoshenko beam model and receptance coupling for the prediction of tool point FRF. International Journal of Machine Tools and Manufacture 2006;46(15):1901–12.
[15] Movahhedy MR, Gerami JM. Prediction of spindle dynamics in milling by substructure coupling. International Journal of Machine Tools and Manufacture 2006;46(3–4):243–51.
[16] Budak E, Ertürk A, Özgüven HN. A modeling approach for analysis and improvement of spindle-holder-tool assembly dynamics. CIRP Annals – Manufacturing Technology 2006;55(1):369–72.
[17] Schmitz T, Powell K, Won D, Duncan GS, Sawyer WG, Ziegert J. Shrink fit tool holder connection stiffness/damping modeling for frequency response prediction in milling. International Journal of Machine Tools and Manufacture 2007;47(9):1368–80.
[18] Cheng C-H, Schmitz T, Duncan GS. Rotating tool point frequency response prediction using RCSA. Machining Science and Technology 2007;11(3):433–46.
[19] Ertürk A, Özgüven HN, Budak E. Effect analysis of bearing and interface dynamics on tool point FRF for chatter stability in machine tools by using a new analytical model for spindle-tool assemblies. International Journal of Machine Tools and Manufacture 2007;47(1):23–32.
[20] Ertürk A, Budak E, Özgüven HN. Selection of design and operational parameters in spindle-holder-tool assemblies for maximum chatter stability by using a new analytical model. International Journal of Machine Tools and Manufacture 2007;47(9):1401–9.
[21] Namazi M, Altintas Y, Abe T, Rajapakse N. Modeling and identification of tool holder–spindle interface dynamics. International Journal of Machine Tools and Manufacture 2007;47(9):1333–41.
[22] Ahmadi K, Ahmadian H. Modelling machine tool dynamics using a distributed parameter tool–holder joint interface. International Journal of Machine Tools and Manufacture 2007;47(12–13):1916–28.
[23] Park S, Chae J. Joint identification of modular tools using a novel receptance coupling method. The International Journal of Advanced Manufacturing Technology 2007;35(11–12):1251–62.
[24] Filiz S, Cheng C-H, Powell K, Schmitz T, Ozdoganlar O. An improved tool–holder model for RCSA tool-point frequency response prediction. Precision Engineering 2009;33:26–36.
[25] Özşahin O, Ertürk A, Özgüven HN, Budak E. A closed-form approach for identification of dynamical contact parameters in spindle-holder-tool assemblies. International Journal of Machine Tools and Manufacture 2009;49(1):25–35.
[26] Sattinger S. A method for experimentally determining rotational mobilities of structures. Shock and Vibration Bulletin 1980;50:17–27.
[27] Duarte MLM, Ewins DJ. Rotational degrees of freedom for structural coupling analysis via finite-difference technique with residual compensation. Mechanical Systems and Signal Processing 1999;14(2):205–27.
[28] Bishop RED, Johnson DC. The mechanics of vibration. Cambridge, UK: Cambridge University Press; 1960.
[29] Blevins R. Formulas for natural frequency and mode shape. Malabar, FL: Kreiger Publishing Co.; 2001.